

ON THE ANISOTROPIC ATTENUATION BEHAVIOR OF THE FLEXURE MODE OF CARBON FIBER COMPOSITES^{+,*}

B. Burks¹, M. A. Hamstad¹

¹ Structural Materials Group, National Institute of Standards and Technology (NIST)
325 Broadway, Mailstop 853, Boulder, CO 80305

* Corresponding author (brian.burks@nist.gov)

Keywords: *attenuation, FEM, flexure mode, stress wave propagation, time-frequency analysis*

1 Introduction

In past years a trend in Modal Acoustic Emission (MAE) and guided wave ultrasonic inspection has arisen in which researchers have used numeric techniques to guide the analysis of experimental NDE measurements. The finite element (FE) method has been successfully applied to the simulation of transient stress waves, facilitating the identification of deformation mechanisms occurring within fiber reinforced composites [1, 2]. Additionally, Sause has used simulation to investigate the effects of holes, rivets, and interlaminar delaminations on the propagation and scattering characteristics of the fundamental Lamb modes occurring within unidirectional carbon fiber composites (CFC) [3].

To extend the utility of numeric techniques for investigating large composite structures (e.g. using simulation to perform probability of detection studies) the effect of wave attenuation in the far-field must be considered. Castaings et al. have successfully modeled material attenuation in the near-field for the 0° direction. Their 2-dimensional work assumed a plane strain formalism, using complex plate constants coupled with frequency domain harmonic analyses and an inverse Fast Fourier Transform (iFFT) [4]. However, the applicability of such an approach in capturing the anisotropic attenuation material behavior in a fully 3-dimensional analysis is unknown at present, as is the utility when considering broadband sources (e.g., acoustic emissions). Experimentally, the attenuation characteristics of the fundamental antisymmetric (A_0 , or flexure) mode of polymer matrix composite (PMC) plates has been investigated [5, 6], yet the frequency dependent nature of attenuation was neglected. A recent study has alluded to this [6], with results forthcoming.

In light of the preceding discussion, the aim of this study was two-fold: to measure the frequency dependent far-field attenuation coefficient of the A_0 mode of a unidirectional CFC in both the 0° and 90° directions, and secondly, to develop a method of tuning a finite element model to match the frequency specific far-field attenuation coefficient of the A_0 mode in both principal directions.

2 Methods

2.1 Experimental

A unidirectional ($[0]_8$) CFC (T300 fibers/epoxy matrix, approximate volume fraction of fibers = 60%) plate of dimensions 1800 mm (0° direction) x 600 mm (90° direction) x 1.14 mm thick was used in the present study. The lateral dimensions of the plate facilitated waveforms free of initial edge reflections. Out-of-plane surface displacements were measured by use of a wideband sensor with displacement-type response, the design and characteristics of which are described in [7]. Sensors were spring mounted to the plate surface via custom fixtures, with the coupling between the plate and the piezoelectric element of the transducer enhanced by the use of vacuum grease. By spring mounting the sensors, consistent coupling was achieved for different propagation distances. Of paramount importance to this study, the sensor had a reasonably flat-with-frequency response at frequencies down to approximately 40 kHz.

A pencil lead break (PLB) of 0.3 mm 2H lead on the top surface of the plate was used as a broadband point excitation source. Waveforms having 4096 points were recorded using a digital oscilloscope at a sampling rate of 10 MHz. The oscilloscope used in the study had 14 bit vertical resolution. A resonant sensor placed 25 mm away in the 0° direction from the PLB location was used as a triggering sensor.

⁺ Contribution of NIST, an agency of the US government; not subject to copyright in the United States.

^{*} Commercial instruments, software, or materials are identified only for scientific completeness. In no case does such identification imply recommendation or endorsement by the National Institute of Standards and Technology, nor does it imply that the products identified are necessarily the best available for the purpose.

Three waveforms at each location were recorded in increments of 25 mm over distances of 100 mm – 500 mm (0° direction), and 100 mm – 300 mm (90° direction).

2.2 Numerical

To simulate the transient stress wave propagation within the unidirectional CFC, a computationally efficient finite element (FE) model was developed, as shown in Fig. 1, and solved using the multi-physics software package Abaqus/Explicit.

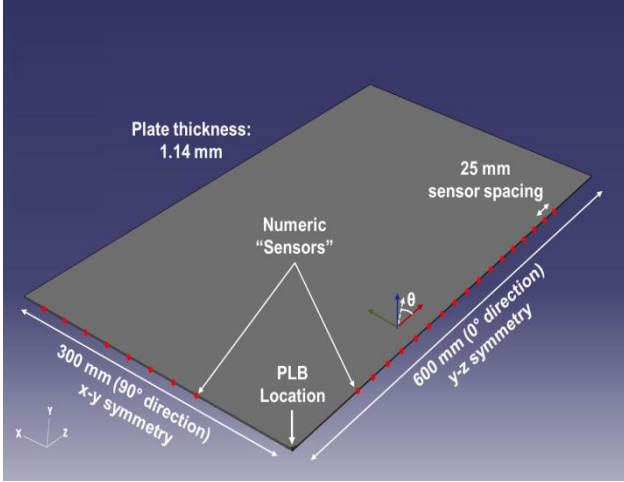


Fig. 1 The FE model with dimensions and features.

The governing partial differential equation for the finite element framework (formulated from the virtual work done by an arbitrary virtual velocity field, $\delta \mathbf{v}$) is stated as

$$\int_V \boldsymbol{\sigma} : \delta \mathbf{D} dV = \int_S \delta \mathbf{v} \cdot \mathbf{t} dS + \int_V \delta \mathbf{v} \cdot \mathbf{f} dV, \quad (1)$$

where \mathbf{t} is the surface traction vector, \mathbf{f} is the body force vector, $\boldsymbol{\sigma}$ is the true stress vector, and $\delta \mathbf{D}$ is the virtual strain rate [8].

Forward advancement of the finite element model in time was calculated in an explicit manner. Thus, the time step used for the analyses conformed to the standard time step limitation (i.e., the time step of an increment must be smaller than the period of time taken for a dilatational wave to traverse the shortest length of an element). As will be elaborated upon in Section 3.2, when more damping was incorporated into the analyses the allowable time step had to be reduced in order for the analyses to remain stable. The use of a lumped mass matrix formulation in conjunction with the explicit central difference

operator used in Abaqus/Explicit resulted in a computationally efficient means of studying the transient dynamic stress wave propagation within the CFC plate.

From symmetry considerations, a one-quarter volume model was utilized to reduce computational expense. The model consisted of first order reduced integration hexahedral elements, which had an element size of 500 μm x 500 μm in-plane x 190.5 μm through the thickness; this element size was adequate for investigation of the frequencies of interest in this study.

Table 1 Material properties used for FE simulations.

Property	Value
C_{11} [GPa]	122.5
$C_{22} = C_{33}$ [GPa]	8.7
$C_{12} = C_{13}$ [GPa]	4.1
C_{23} [GPa]	4.9
C_{44} [GPa]	1.9
$C_{55} = C_{66}$ [GPa]	3.5
ρ [kg/m^3]	1560

A linear elastic anisotropic constitutive model was used for the simulations. The material was modeled as a transversely isotropic elastic solid with material constants (C_{ij}) and density (ρ) as defined in Table 1. Measured material properties (moduli: E_{11} and E_{22} , and Poisson's ratios: ν_{12} and ν_{21}) obtained from tensile tests performed on specimens in a 0° and 90° orientation with bonded rosettes were found to be in good agreement with the values reported in Table 1.

PLBs were simulated by the application of a concentrated load being applied in the out-of-plane direction. The total force release was 1N, while the temporal shape of the source rise function was a cosine bell with a rise time of 1 μs . Out-of-plane displacements were recorded at nodal locations at the distances described in Section 2.1, and were used for direct comparison to the experimental waveforms.

In order to tune the finite element model to match the experimentally measured attenuation coefficient, Rayleigh damping was employed. Rayleigh damping introduces damping, $[C]$ into the model by using contributions from both the mass $[M]$ and stiffness $[K]$ matrices of an element, i.e.

$$[C] = \alpha[M] + \beta[K], \quad (2)$$

where α and β are the mass and stiffness proportional Rayleigh constants, respectively [8].

2.3 Attenuation and signal processing

The far-field attenuation process is well described by an exponential decay

$$A = A_0 \exp(-T_\theta r), \quad (3)$$

where A is the amplitude, A_0 is a material and source specific constant, r is the propagation distance, and T_θ is the attenuation coefficient in the θ direction. In light of the broadband sensor's characteristics described in Section 2.1, all waveforms (experimental and numeric) were post-processed with a fourth order Butterworth filter having a pass band between 40 kHz and 1500 kHz. Such post-processing facilitated comparison between experimental sensor output voltage and numerically calculated displacement signals.

Subsequently, the Choi-Williams distributions (CWD) of all filtered waveforms were then calculated with fixed scaling parameters, over a frequency range of 0 kHz to 300 kHz using 112 terms in the damping summation, an exponential damping parameter equal to 20, and a frequency step of 1.2 kHz. Hamstad provides an excellent discussion of the advantages of the Choi-Williams distribution over continuous wavelets in [9]. The maximum amplitude of the CWD coefficient of the initial arrival portion of the A_0 mode at frequencies of interest were extracted from the CWD, and converted to the Nepers scale. The amplitude (L) on the Nepers scale of a CWD coefficient value (v) relative to a reference value (v_{ref}) is defined as

$$L = \log_e \frac{v}{v_{ref}}. \quad (4)$$

Experimental and numerical attenuation coefficients were determined by using least squares regression of the amplitude (in Nepers) plotted against propagation distance. In this work, frequencies between 50 kHz and 100 kHz were considered due to the fact that every waveform showed strong contributions at these frequencies for all combinations of propagation distance and direction.

3. Results and Discussion

3.1 Experimental

Phase and group velocity dispersion curves for the unidirectional CFC plate with a thickness of 1.14 mm are shown in Fig. 2. Due to the significantly greater stiffness in the 0° direction, both the fundamental symmetric (S_0) and antisymmetric modes show greater wave speeds for the 0° propagation direction in comparison to the 90° propagation direction.

The temporal waveform and corresponding CWD of a signal, excited from a surface PLB, acquired at a propagation distance of 200 mm in the 0° direction are shown in Fig. 3. From Fig. 3 it was observed that the out-of-plane surface PLB excited predominantly the A_0 mode; minimal contributions from the fundamental S_0 mode were observed in the temporal waveform first showing up at approximately $60 \mu\text{s}$. Fig. 4 provides the analogous plot to Fig. 3 for the 90° propagation direction.

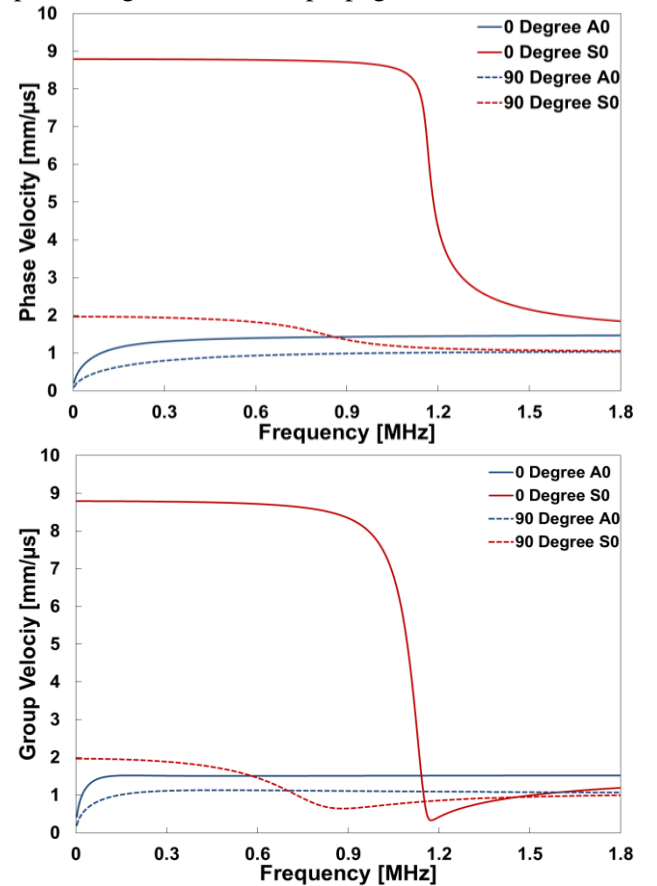


Fig. 2 Phase (top) and group (bottom) velocity dispersion curves for the fundamental modes of the unidirectional ($[0]_s$) CFC plate for the 0° and 90° propagation directions.

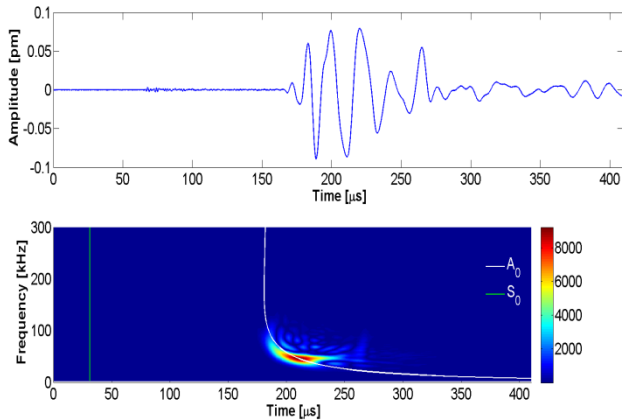


Fig. 3 Temporal waveform (top) and CWD (bottom) of an experimental signal acquired at a propagation distance of 200 mm in 0° direction.

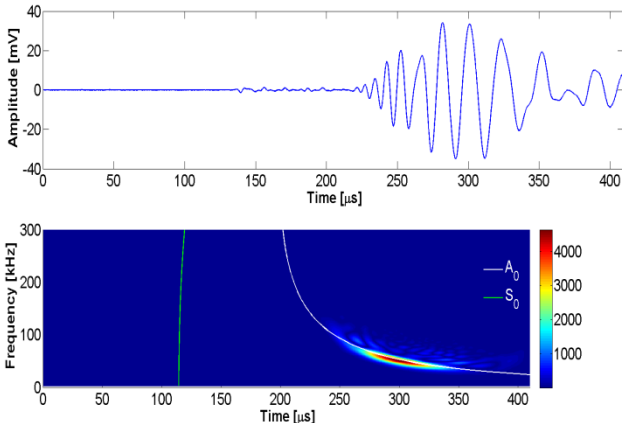


Fig. 4 Temporal waveform (top) and CWD (bottom) of an experimental signal acquired at a propagation distance of 200 mm in 90° direction.

In accordance with the procedure described in Section 2.1, three waveforms at each propagation distance were recorded, their respective CWD's calculated, and the peak intensity value of the initial arrival at a frequency of interest was extracted. As a representative example, Fig. 5 presents results for the 0° propagation direction at a frequency of 75 kHz. From the linear least squares regression the experimental far-field attenuation coefficient (T_0) was found to be (18.1 ± 1.4) Np/m (values reported mean \pm 95 % confidence interval).

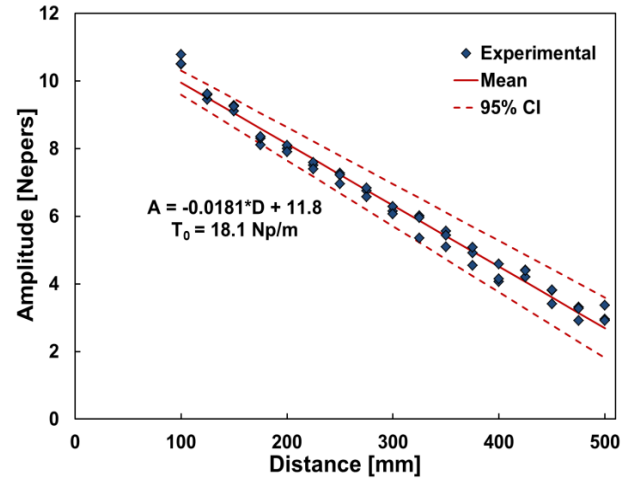


Fig. 5 Measured attenuation coefficient (with the 95% confidence interval) for the 0° propagation direction at a frequency of 75 kHz.

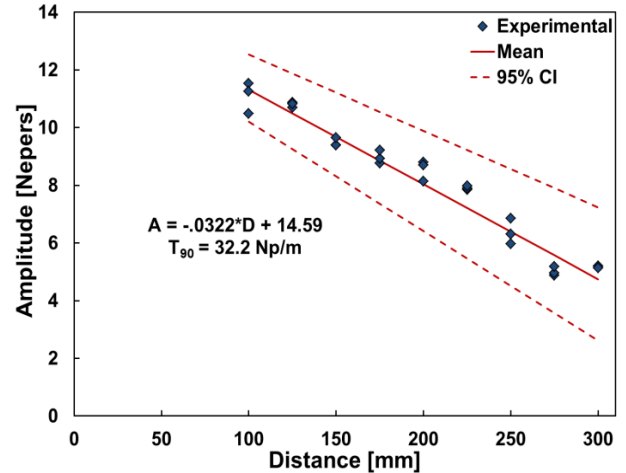


Fig. 6 Measured attenuation coefficient (with the 95% confidence interval) for the 90° propagation direction at a frequency of 75 kHz.

Illustrative results for the attenuation coefficient at a frequency of 75 kHz for the 90° propagation direction are shown in Fig. 6. For the 90° propagation direction, T_{90} was found to be (32.2 ± 2.9) Np/m. In comparing the attenuation behavior in the 0° and the 90° direction at 75 kHz, it is clear that attenuation was found to be substantially greater in the 90° direction than in the 0° direction. Such observations are in agreement with most of those of [6], although in that work the frequency specific nature of attenuation was not considered, and resonant transducers were used.

Results for the mean attenuation coefficient and 95 % confidence interval for both propagation

directions (T_0 and T_{90}) at frequencies of 50 kHz, 75 kHz, 85 kHz, and 100 kHz are summarized in Table 2. It was observed that in both principal propagation directions that the attenuation coefficients increased with increasing frequency. Moreover, the attenuation coefficient in the 90° direction was approximately a factor of two greater than that in the 0° direction for the frequencies considered in this work, and it increased more rapidly with frequency increases as compared to 0° results.

Table 2 Summary of the experimentally measured frequency specific far-field attenuation coefficients of the A_0 mode for unidirectional CFC plate.

Frequency [kHz]	T_0 [Np/m]	T_{90} [Np/m]
50	15.2 ± 1.6	23.2 ± 3.3
75	18.1 ± 1.4	32.2 ± 2.9
85	19.4 ± 1.1	37.6 ± 2.6
100	19.5 ± 1.3	44.2 ± 3.2

3.2 Numerical

As a means of providing insight into how the anisotropic quasi-Lamb waves propagate within the unidirectional CFC plate, a progression of the out-of-plane (u_y) displacement field for a model simulating a surface PLB with no material damping is shown in Fig. 7, with all pertinent wave modes identified. Note that the coloring scale has been augmented as to reveal the structure of the quasi-longitudinal and quasi-shear horizontal (SH) modes that have significantly reduced out-of-plane displacement amplitudes in comparison to the quasi-shear vertical (SV) mode. For monoclinic and higher symmetry materials (up to but not including isotropic symmetry), pure modes do not exist except in the case of propagation along principal directions [10]. Thus, in the context of this study the use of the A_0 nomenclature in place of quasi-SV is consistent with the literature for the 0° and 90° propagation directions, but is understood not to be a pure mode due to material anisotropy for all other values of θ .

To tune the far-field attenuation behavior of the FE model to match that of the experimental study, only the stiffness proportional damping term in eqn. (2) was utilized. This was done in light of the relationship between the critical damping factor (ζ) added to the model, angular frequency (ω), and the mass (α) and stiffness (β) proportional damping parameters [8]

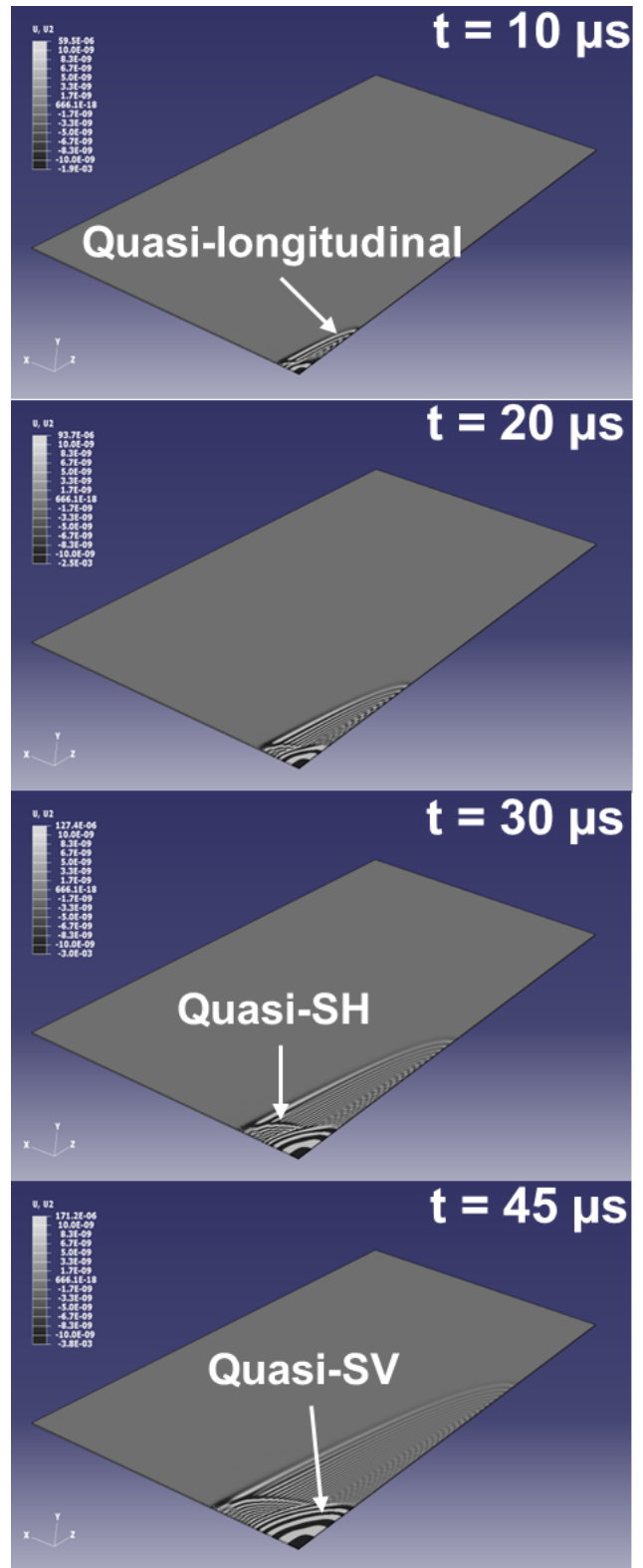


Fig. 7 Time progression of the out-of-plane displacement field, elucidating the mode shapes that propagate due to a surface PLB.

$$\xi = \frac{\alpha}{2\omega} + \frac{\beta\omega}{2}. \quad (5)$$

Inspection of eqn. (5) shows that the amount of damping introduced into the model is inversely proportional to frequency for mass proportional damping; such behavior is in general not representative of material behavior in the far-field. Thus, only stiffness proportional damping was employed due to the increased damping incorporated into the model with respect to frequency.

Examination of Figs. 3 and 4 revealed that the A_0 mode had significant energy at 75 kHz in both principal propagation directions. For this reason, the numeric model was tuned at 75 kHz in the 0° direction to match the experimental attenuation coefficient (T_0), while also monitoring how the attenuation coefficient in the 90° propagation (T_{90}) direction responded.

The effect of β on the simulated far-field attenuation coefficients in both principal directions is shown in Fig. 8. In light of the results presented in Fig. 8 and Table 2, a β value of $9.33\text{E-}08$ s would tune the numerical T_0 value to identically match the experimentally measured mean value. Simulation with this damping parameter confirmed this supposition, as shown in Fig. 9. As an aside, it is pointed out that with the use of β proportional damping and this particular combination of mesh density and material parameters, the stable time increment had to be decreased from 10 ns ($\beta = 0$ s) to 4 ns ($\beta = 9.33\text{E-}08$ s); such a decrease in the stable time increment resulted in analysis times that were roughly 2x longer than the undamped analysis.

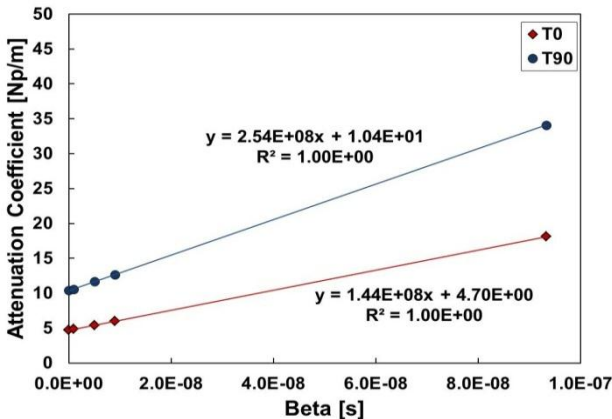


Fig. 8 Effect of β on the attenuation coefficient in both principal directions.

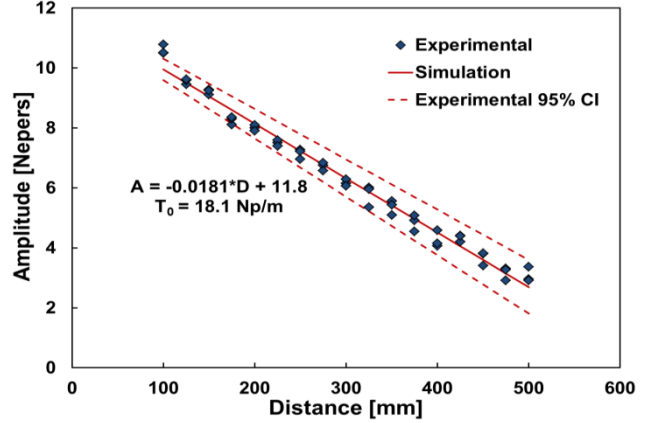


Fig. 9 Comparison of experimental data and the attenuation coefficient predicted via simulation using $\beta = 9.33\text{E-}08$ s in the 0° propagation direction at a frequency of 75 kHz.

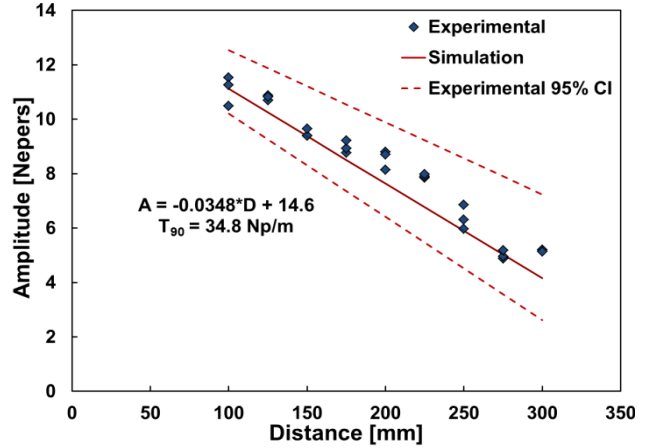


Fig. 10 Comparison of experimental data and the attenuation coefficient predicted via simulation using $\beta = 9.33\text{E-}08$ s in the 90° propagation direction at a frequency of 75 kHz.

Moreover, with $\beta = 9.33\text{E-}08$ s the transverse attenuation coefficient, T_{90} , was found to have a simulated value of 34.8 Np/m. A comparison of simulated transverse attenuation data and the experimentally measured data is presented in Fig. 10. By tuning the attenuation behavior of the finite element model in the 0° direction, the response of the numerical model in the principal transverse direction closely matched that of the experimentally measured attenuation coefficient. Such behavior indicates that the model is accurately accounting for all forms of attenuation not related to material attenuation (i.e., velocity dispersion, and geometric spreading). Moreover, through the technique developed in this work the use of stiffness

proportional Rayleigh damping was able to account for the effects of material attenuation in the far-field for transient dynamic analyses.

Looking at the temporal and time-frequency response of the tuned model, Fig. 11 presents the simulated waveform and CWD at a propagation distance of 200 mm in the 0° direction. In comparing the experimental waveform and CWD (Fig. 3) to the numerically simulated waveform and CWD (Fig. 11) reasonable agreement was observed, when account is taken for the fall-off of the lower frequency response of the experimental sensor when comparing the waveforms [7].

Fig. 12 presents the numerically simulated waveform and CWD of the tuned model in the 90° direction at a propagation distance of 200 mm. Outstanding agreement (again tempered by the reduced low frequency response of the experimental sensor compared to the “perfect” response of the numerical model) between the experimental waveform and CWD (Fig. 4) and the numerical waveform and CWD (Fig. 12) were noted.

To further investigate the use of Rayleigh damping and the numerically simulated attenuation behavior, the frequency specific nature of attenuation was examined. To this end, the attenuation coefficients at 50 kHz, 75 Hz, 85 kHz, and 100 kHz for the numerical model tuned at 75 kHz were extracted with the results summarized in Table 3. Comparing the values presented in Tables 2 and 3, mixed results were observed. In looking at the attenuation coefficient in the 90° propagation direction, excellent agreement was observed for all values of frequency considered. However, in the 0° propagation direction (direction used for tuning) reasonable agreement of the simulation attenuation coefficient with the experimentally measured attenuation coefficient was only observed for a frequency band of approximately ± 10 kHz, centered about the tuning frequency (75 kHz); outside of this bandwidth simulation results were found to under-damp the attenuation behavior for lower frequencies, while over-damping for higher frequencies.

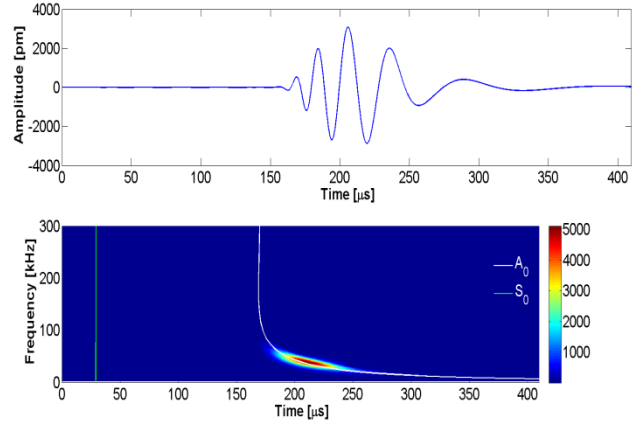


Fig. 11 Temporal waveform (top) and CWD (bottom) of a numerical signal acquired at a propagation distance of 200 mm in 0° direction.

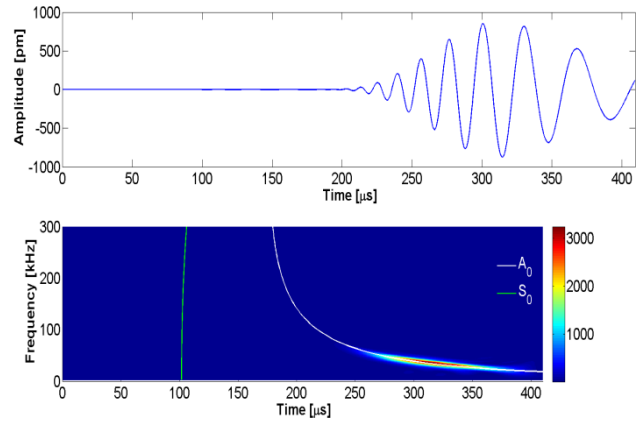


Fig. 12 Temporal waveform (top) and CWD (bottom) of a numerical signal acquired at a propagation distance of 200 mm in 90° direction.

Table 3 Summary of the frequency specific far-field attenuation coefficients of the A_0 mode for the tuned FE model of the unidirectional CFC plate.

Frequency [kHz]	T_0 [Np/m]	T_{90} [Np/m]
50	10.9	22.5
75	18.1	34.1
85	22.2	39.9
100	35.3	47.4

3.3 General Discussion

From the results presented in Sections 3.1 and 3.2, agreement between the experimentally measured far-field attenuation coefficient of a plate type unidirectional CFC and a tuned numerical model were observed. It was shown that through the use of stiffness proportional Rayleigh damping, the numeric model could be tuned in the 0° propagation

direction to exactly match the experimental attenuation behavior at a frequency of interest. In addition, it was found that this procedure resulted in excellent agreement between experimental and numerical values for the other principal attenuation coefficient (i.e., T_{90}). When considering frequencies ± 10 kHz outside of the center tuned frequency, divergent results were observed for the 0° propagation direction. However, numerically simulated results in the principal transverse propagation direction exhibited good agreement with experimental values for all frequencies considered.

The cause for the over-damping in the 0° propagation direction is evident when considering how the stiffness proportional damping is introduced into the finite element model. Stiffness proportional damping is introduced into the model as a damping stress, σ_D , and is defined as

$$\sigma_D = \beta C^{el} \dot{\epsilon}, \quad (6)$$

in which C^{el} is the material's current elastic stiffness matrix, and $\dot{\epsilon}$ is the strain rate [8]. At each time step the calculated damping stress is superimposed on the stress resulting from the material's constitutive response. Examination of eqn. (6) indicates that the component of damping stress in the axial direction will be far greater than the damping components of stress in the transverse propagation direction due to the considerably larger value of C_{11} as compared to $C_{22} = C_{33}$ (given in Table 1).

To further enhance the ability to account for material attenuation in transient dynamic simulations and rectify the lack of agreement over a broad frequency range observed for the 0° propagation direction, two solutions appear possible. The first solution would be to implement an anisotropic stiffness proportional Rayleigh vector. Through this approach each component of the stiffness proportional Rayleigh vector could be independently tuned to match experimental data. Such a technique would be analogous to the procedure developed in this work, with the added layer of complexity of independent tuning directions. Such a solution would likely be a viable approach for single mode analyses.

However, the previously proposed approach would lack the ability to accurately capture the attenuation behavior of multiple modes in the same analysis. Because different modes have different attenuation

coefficients at the same frequencies, the use of an anisotropic Rayleigh vector may be ineffective in accurately capturing the attenuation behavior.

The second alternative to accurately model the anisotropic attenuation behavior of a broadband multiple mode source in a transient dynamic analysis would be to accurately model the viscoelastic response of the material under study. Such an approach may be viable; however, obtaining viscoelastic properties of the material under study at the ultrasonic frequencies (or alternatively time intervals) of interest is not trivial. Work is currently under way in developing such a method to evaluate the efficacy of such an approach.

4. Conclusion

In this study two techniques were developed to investigate the far-field attenuation behavior of a unidirectional CFC plate. Experimentally a broadband source was used to primarily excite the A_0 mode with a time-frequency analysis procedure used to determine the frequency dependent anisotropic far-field attenuation coefficients.

Subsequently, a transient dynamic finite element model was tuned to match the experimental attenuation behavior at a specific frequency of interest. The technique was found to effectively capture the anisotropic attenuation behavior at the tuning frequency. Moreover, the attenuation behavior in the principal transverse direction of the tuned model was found to agree with experimentally determined attenuation coefficients over the frequency range investigated. In the 0° propagation direction, the tuned model's response was less robust and only agreed with experimental attenuation values over a bandwidth of approximately ± 10 kHz centered about the tuning frequency.

Thus, the performance of the current numerical approach was adequate in accounting for the anisotropic attenuation behavior of narrowband signals (quite useful for example on Hanning windowed ultrasonic tone bursts) that intend to excite only a single wave mode. However, to accurately account for broadband sources with the potential of exciting multiple modes of propagation, a more robust technique is required. Suitable techniques have been outlined, with one technique being developed to evaluate the efficacy.

Acknowledgements

This work used the Extreme Science and Engineering Discovery Environment (XSEDE), which is supported by National Science Foundation grant number OCI-1053575. Also, this research was performed while Brian Burks held a National Research Council Research Associateship Award at the National Institute of Standards and Technology (NIST) in Boulder, CO.

References

- [1] M. Sause, S. Horn, "Simulation of acoustic emission in planar carbon fiber reinforced plastic specimens". *Journal of Nondestructive Evaluation*, Vol. 29, pp 123-142, 2010.
- [2] B. Burks, M. Kumosa, "A modal acoustic emission signal classification scheme derived from finite element simulation". *International Journal of Damage Mechanics*, accepted, 2013.
- [3] M. Sause, S. Horn, "Influence of internal discontinuities on ultrasonic signal propagation in carbon fiber reinforced plastics". *Proceedings of the 30th European Conference on Acoustic Emission Testing*, Granada, Spain, 2012.
- [4] M. Castaings, C. Bacon, B. Hosten, M. Predoi, "Finite element predictions for the dynamic response of thermo-viscoelastic material structures". *Journal of Acoustical Society of America*, Vol. 115, No.3, pp 1125-1133, 2004.
- [5] W. Prosser, "Applications of advanced, waveform based AE techniques for testing composite materials". *Proceedings of the SPIE Conference*, Scottsdale, AZ, pp. 146-153, 1996.
- [6] A. Gallego, and K. Ono, "An improved acousto-ultrasonic scheme with Lamb wave mode separation and damping factor in CFRP". *Proceedings of the 30th European Conference of Acoustic Emission Testing*, Granada, Spain, 2012.
- [7] M. Hamstad, "Improved signal-to-noise wideband acoustic/ultrasonic contact displacement sensors for wood and polymers". *Wood and Fiber Science*, Vol. 29, No. 3, pp.239-248, 1997.
- [8] Abaqus. Abaqus v.6.9 Documentation. s.l. : Dassault Systemes; 2009.
- [9] M. Hamstad, "Comparison of wavelet transform and Choi-Williams distribution to determine group velocities for different acoustic emission sensors". *Journal of Acoustic Emission*, Vol. 26, pp. 40 – 59, 2008.
- [10] A. Nayfeh "Wave propagation in layered anisotropic media with applications to composites". 1st edition, Elsevier, 1995.